

POLITECNICO DI TORINO
Repository ISTITUZIONALE

Identifying multiple-scattering-affected profiles in CloudSat observations over the oceans

Original

Identifying multiple-scattering-affected profiles in CloudSat observations over the oceans / Battaglia, A.; Haynes, J. M.; L'Ecuyer, T.; Simmer, C.. - In: JOURNAL OF GEOPHYSICAL RESEARCH. - ISSN 2156-2202. - 114:8(2009). [10.1029/2008JD009960]

Availability:

This version is available at: 11583/2807432 since: 2020-03-30T16:23:00Z

Publisher:

Blackwell Publishing Ltd

Published

DOI:10.1029/2008JD009960

Terms of use:

This article is made available under terms and conditions as specified in the corresponding bibliographic description in the repository

Publisher copyright

(Article begins on next page)

Identifying multiple-scattering-affected profiles in CloudSat observations over the oceans

A. Battaglia,¹ J. M. Haynes,² T. L'Ecuyer,² and C. Simmer¹

Received 7 February 2008; revised 3 September 2008; accepted 16 September 2008; published 10 December 2008.

[1] Multiple scattering strongly affects the CloudSat Profiling Radar reflectivity when the satellite is overpassing moderate and heavy precipitation systems. Therefore it is important to identify profiles that may be contaminated by multiple scattering prior to interpreting the results of any application that involves the use of CloudSat data in raining scenes. On the basis of analysis of multiple-scattering Monte Carlo reflectivity simulations applied to cloud-resolving model-generated microphysical profiles encompassing a large variety of precipitating systems, a relatively straightforward criterion is proposed for flagging profiles potentially affected by multiple scattering. The path-integrated attenuation, that can be estimated from CloudSat's 2B-GEOPROF product, can be used to identify four multiple-scattering regimes: (1) the single scattering approximation is applicable to the entire Z-profile; (2) the single scattering approximation is unreliable but the second order of scattering approximation is valid; (3) the second order of scattering approximation is not valid owing to higher order of multiple-scattering effects which, however, do not affect the surface reference technique-based path-integrated attenuation estimates; and (4) the multiple scattering is affecting the surface return as well, thus spoiling the path-integrated attenuation estimates. Operational path-integrated attenuation thresholds for each of these regimes are then applied to the CloudSat data set over the global oceans, where path-integrated attenuation estimations are more accurate than over land. Case studies and global statistics of the occurrence of multiple scattering are presented: for ocean pixels, around 80% (90%) of the profiles identified as rainy can be treated in the single scattering (second order of scattering) approximation. A threshold value around 20 dB for the one-way path-integrated attenuation is suggested for the applicability of the surface reference technique to the CloudSat Profiling Radar system. This roughly corresponds to 96.5% of the rainy pixels. Owing to the different precipitation regimes, results are strongly regionally and seasonally dependent. For instance in the Inter-Tropical Convergence Zone a not negligible fraction of the raining pixels requires either second-order (10–15%) or higher-order scattering ($\sim 10\%$) to accurately model the observed reflectivity profile.

Citation: Battaglia, A., J. M. Haynes, T. L'Ecuyer, and C. Simmer (2008), Identifying multiple-scattering-affected profiles in CloudSat observations over the oceans, *J. Geophys. Res.*, 113, D00A17, doi:10.1029/2008JD009960.

1. Introduction

[2] The CloudSat satellite has been in orbit since 26 April 2006 and its 94.0 GHz Cloud Profiling Radar (CPR) has been successfully acquiring data since 20 May 2006. According to its acronym, the instrument is principally devoted to a better understanding of the vertical distribution of clouds [Stephens *et al.*, 2002; Haynes and Stephens, 2007; Mace *et al.*, 2007]. In addition, thanks to its spatial resolution (1.4/1.8 km along/cross track [Tanelli *et al.*, 2008]) which is higher than other spaceborne radars (e.g.,

the Tropical Rainfall Measuring Mission Precipitation Radar [Kummerow *et al.*, 1998] or those planned for the Global Precipitation Measurement [Iguchi *et al.*, 2002]), the CPR represents a unique precipitation detector, suited for better understanding the transition between clouds and precipitation, be it drizzle, rain or snowfall. Owing to its nadir pointing configuration the CPR can however provide only a two-dimensional cut through the systems under observation; owing to its single frequency, the CPR has difficulties in particle sizing; and finally owing to its high frequency the CPR is prone to attenuation problems. Despite the latter problems, when browsing the images at http://www.cloudsat.cira.colostate.edu/data_dist/OrderData.php or looking at some case studies (<http://www.cloudsat.cira.colostate.edu/CaseStudies.php> or Mitrescu *et al.* [2008, Figures 2, 3, and 4]), the CPR precipitation echo signal seems to remain above the minimum detection threshold

¹Meteorological Institute, University of Bonn, Bonn, Germany.

²Department of Atmospheric Sciences, Colorado State University, Fort Collins, Colorado, USA.

Table 1. PIA_{hydro} Thresholds for SS, SOS, and SRT Validity^a

Freezing Level	SS Validity	SOSA Validity	SRT Validity
FL < 3 km	3.5–4.9 (71.3–80.6%)	8.0–11.0 (91.1–95.5%)	16.9–18.6 (98.6–99.0%)
3 < FL < 5 km	5.8–8.0 (82.2–87.8%)	8.9–13.8 (89.3–94.2%)	19.4–19.6 (96.9–97.0%)
FL > 5 km	5.7–9.1 (78.1–86.0%)	14.5–14.9 (91.7–92.0%)	20.9–21.3 (95.2–95.4%)
All FL	79.7–86.5%	90.5–93.3%	96.4–96.6%

^aThresholds are given in decibels. In each box the first number corresponds to the 99% POD level; the second one is found by maximizing the ETS. The fraction of CloudSat rainy profiles fulfilling the condition on the PIA_{hydro} is indicated in parentheses.

estimated to be between –30 dBZ and –31 dBZ [Tanelli et al., 2008] (which can be assumed as an equivalent threshold also when the signal includes the surface echo) down to the ground for a large number of cases, even when the satellite overpassed intense precipitating systems (e.g., tropical storms, squall lines or hurricanes). Loss of signal (including surface echoes) occurs for only around 0.023% of the total and 0.3% of the oceanic profiles identified as rainy case. The presence of rain is determined from CloudSat observations using the combined path-integrated attenuation and near-surface reflectivity method of J. M. Haynes et al. (Rainfall retrieval over the ocean with spaceborne W-band radar, submitted to *Journal of Geophysical Research*, 2008), delineating the rain as “possible” through “definite” categories described in their Table 1. This percentage far exceeds the expectations based on single scattering (SS hereafter) theory, which forecasts strong attenuation for such an high-frequency system [e.g., Lhermitte, 1990]. For instance, a Marshall and Palmer distributed 10 (20) mm/h rain leads to an attenuation coefficient of 8.2 (13.4) dB/km: 4- (2.5-) km-thick rain layers are therefore sufficient to produce a two-way integrated attenuation of more than 60 dB, which would suffice to attenuate the surface signal below the minimum sensitivity. The attenuation further increases when including the absorbing effects of atmospheric gases and cloud liquid water [Pujol et al., 2007].

[3] As demonstrated by numerical simulations of different authors [Marzano et al., 2003; Kobayashi et al., 2005, 2007; Battaglia et al., 2005, 2006a, 2006b, 2007], the presence of multiple scattering (MS hereafter) effects in high-frequency spaceborne radars can partially compensate for the attenuation losses, thus producing a signal even in otherwise below minimum sensitivity regions. Basically radiation can be scattered out (in) and reenter (remain in) the beam at a later point in time through MS. This means that the power returned from a given radar pulse volume may include both the SS backscatter from particles within that volume and power from radiation that underwent MS [see Battaglia et al., 2006a, Figure 1]. This should certainly be the case when profiles of highly developed precipitating system are observed by a radar in the CloudSat configuration [Battaglia et al., 2007]. Battaglia and Simmer [2008] have derived additional evidences of MS in CloudSat data when looking at the return from ranges corresponding to the surface and longer; on the basis of simulations for a simple microphysical flux-preserving model three behaviors have been identified: (1) at low rain rates SS is valid for the whole vertical profile; (2) at intermediate rain rates MS is affecting the pixels close to the ground but not yet the surface return; and (3) at high rain rates MS modifies both the largest part of the profile and the surface return. The specific rain-rate thresholds depend on the thickness of the precipitating system and

on its microphysical characteristics. In addition, Battaglia et al. [2008] discussed the range of validity of the second order of scattering (SOS) approximation and concluded that already for surface rain rate of 3–4 mm/h the SOS is likely to produce errors above 3 dB. Therefore SS/SOS approaches are certainly not appropriate to simulate CloudSat profiles except in light rain. For medium-high rain rates, since at W-band the effective reflectivity does not change much with rain rate beyond about 5 mm/hr [Matrosov, 2007], the presence of MS effects will mainly impact the attenuation correction and lead to an underestimate of the rain rate by reducing the path-integrated attenuation (PIA) and the layer-to-layer attenuation corrections inferred from the data. These considerations may significantly impact the quality of CloudSat rain retrievals and underscore the need of first identifying the reflectivity profiles burdened by MS effects by detecting where MS is expected to be possibly present, certainly present or dominant.

[4] MS contamination in the CloudSat signal has been demonstrated by collocated airborne observations. For example Figure 1 (top and middle) shows reflectivities profiles as sensed on 30 July 2007, both by the CloudSat CPR and by the Cloud Radar System (CRS) [Li et al., 2004] deployed on the ER-2 airplane, which is under-flying the CloudSat ground track during the CALIPSO-CloudSat Validation Experiment conducted during July–August 2006 over the mideast United States. Note that the airplane is actually detected by the CloudSat CPR at an altitude of 21 km and at a distance along-track around 225 km. In close vicinity to the perfect collocation point (which excludes the possibility of advection of rain cells during the time gap between the two observations, as it probably happens at an along-track distance of 115 km) both radars are overpassing a highly developed precipitating system. Within that region large differences (>10 dB) between the reflectivities are found close to the surface (see Figure 1, bottom). The CPR reflectivity becomes increasingly larger than the CRS reflectivity in the rainy region; this is a clear evidence of MS enhancement, a phenomenon the amplitude of which is mainly driven by the footprint size [e.g., Battaglia et al., 2005; Kobayashi et al., 2005].

[5] Although an attenuation-based estimation of rain rate has been recently proposed [Matrosov, 2007; Matrosov et al., 2008] the rain profile product from CloudSat is based on the optimal estimation procedure described by L'Ecuyer and Stephens [2002], which synthesizes the spaceborne techniques well-established within the TRMM-PR era [e.g., Kummerow et al., 1998; Iguchi et al., 2000] and implicitly accommodates the slope approach by Matrosov [2007] as well. The backbone of the algorithm is an attenuating radar forward operator; although initially implemented as a SS-based model [see L'Ecuyer and Stephens,

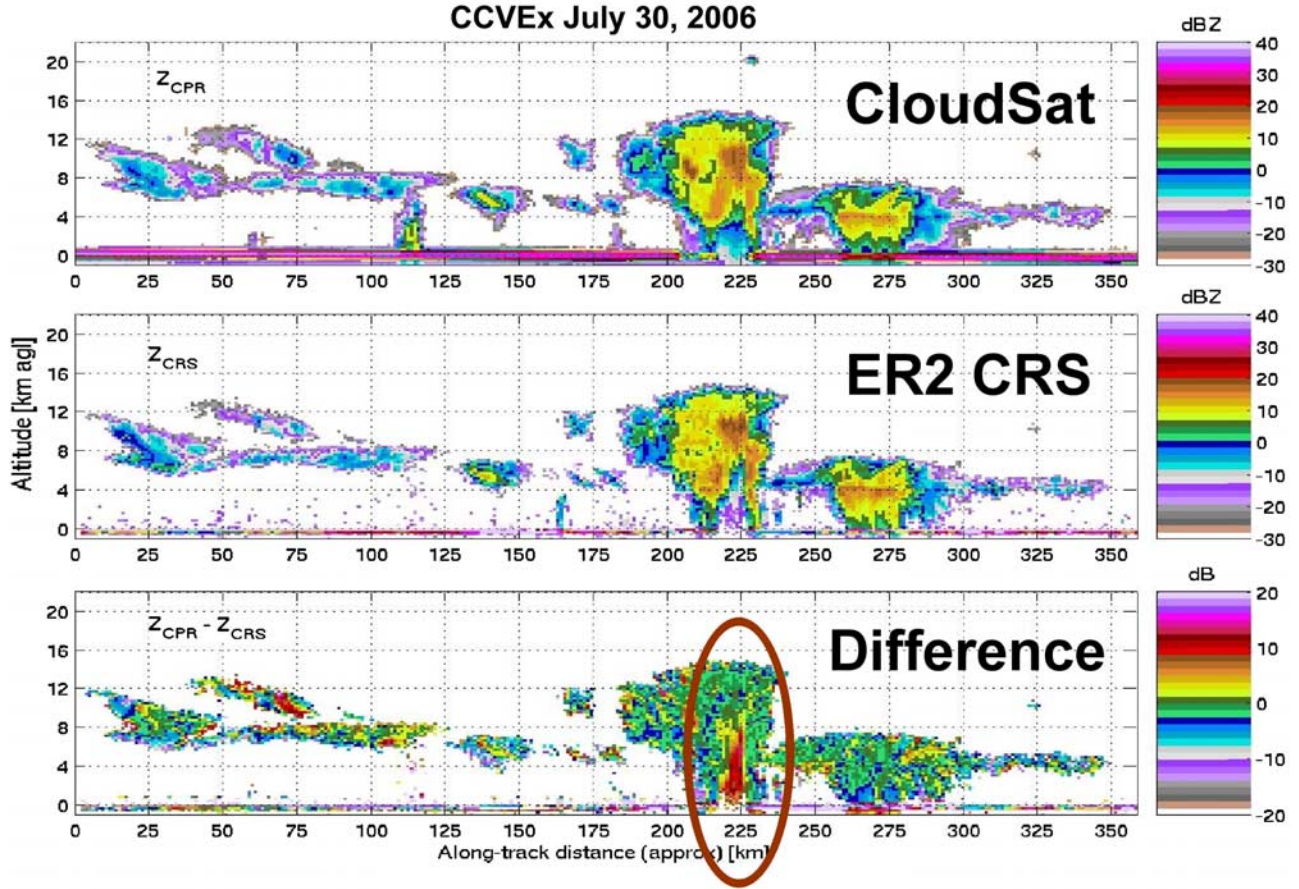


Figure 1. Evidence of multiple-scattering effects from the airborne CloudSat/CALIPSO Validation Experiment (CCVEx). (top) CloudSat radar reflectivity in dBZ ; (middle) ER2-CRS radar reflectivity in dBZ under flying the CloudSat ground track; and (bottom) difference between the CPR and the CRS reflectivities in decibels. This image, courtesy of S. Tanelli (Jet Propulsion Laboratory, California Institute of Technology), was generated using CRS preliminary calibration data courtesy of G. Heymsfield (NASA/GSFC) and L. Li (GEST). Relative calibration between CPR and CRS has been corrected since, and this image should be regarded as calibrated within 3 dB. The MS signature due to the different footprint sizes is evident well beyond this calibration uncertainty.

2002, section 2] it has the flexibility to include higher orders of scattering. A SOS approximation is under development while the use of fast radar MS models [e.g., Hogan and Battaglia, 2008] is planned for the near future. The method is quite flexible and well-suited for the addition of measurements from other sensors, useful to better retrieve the strongly attenuated rain profiles [see L'Ecuyer and Stephens, 2002, Figures 11–14]. For the CPR such constraints are provided either as total precipitation water paths by microwave radiometers (e.g., AMSR-E is part of the A-Train, but has quite a different footprint size) or as path-integrated attenuation (PIA) retrieved by the radar surface reference technique (SRT) [Meneghini et al., 2000, 2004]. Mitrescu et al. [2007] analyzed the CloudSat surface return PDFs for different surface types and noticed that only over water surfaces the variability can be satisfactorily accounted for by a wind- and sea-surface-temperature-dependent correction and that there are no significant differences between the three configurations of the CloudSat beam with respect to the local zenith. By using the 2B-GEOPROF data product, Haynes and Stephens [2007]

derived the PIA due to hydrometeors (PIA_{hydro} hereafter) as the difference between the values of surface backscatter under precipitating clouds and the value of an equivalent clear sky ocean surface backscatter (which results from subtracting the gas attenuation from the pure surface backscattering). Gaseous attenuation is derived from the available temperature and moisture profiles taken from ECMWF analyses matched to the CPR footprint. By combining all uncertainties PIA_{hydro} can be estimated over ocean within 2 dB. Besides constraining the inversion problem, PIA have been already suggested as indicators of MS [e.g., Battaglia et al., 2007, Figure 8]. Therefore PIA represents the most logical choice for a driving parameter in the identification of MS burdened CloudSat reflectivity profiles, particularly over an oceanic background.

[6] After presenting some numerical simulations, an objective criterion for flagging MS-affected CloudSat profiles (based on PIA estimates and on additional storm characteristic) is proposed in section 2. The operational thresholds are then applied to the available CloudSat data set over sea: case studies and global statistics of the

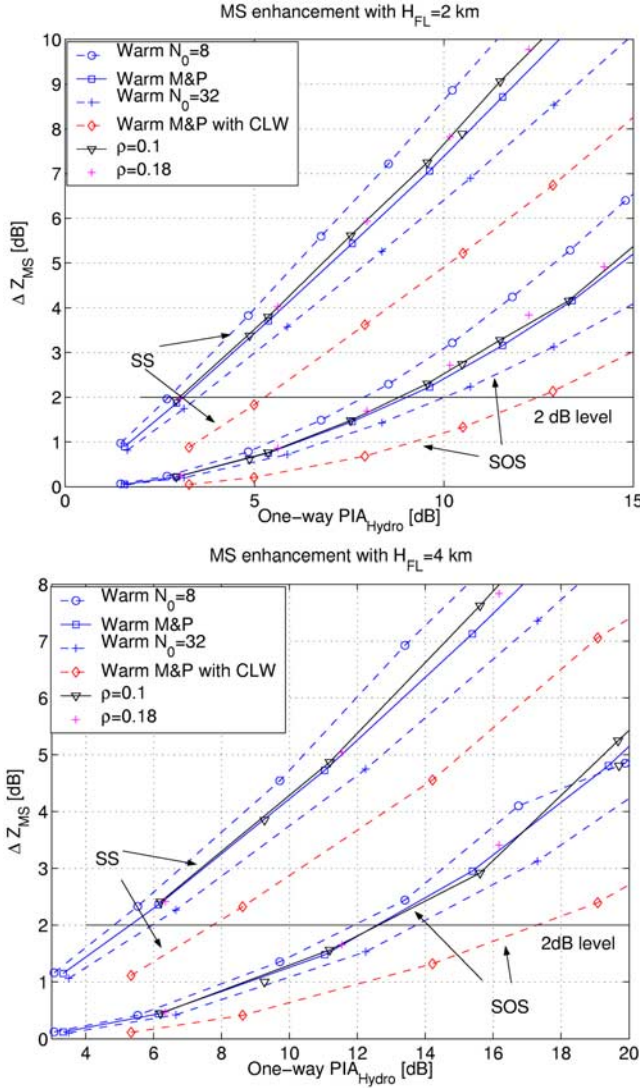


Figure 2. SSA and SOSA error in the return of the range gate close to the surface for vertical flux preserving scenarios with (top) $H_{FL} = 2$ km and (bottom) $H_{FL} = 4$ km. Two groups of curves are plotted: on the left/right side those relative to the SSA/SOSA error. Each group includes six different microphysics profiles as indicated in the legend (see text for details).

occurrence of multiple scattering are reported in section 3. Discussions and conclusions are then drawn in section 4.

2. Criteria for Flagging MS-Burdened Profiles

[7] This work aims at identifying CloudSat pixels which are MS-burdened by an analyses of the characteristics of the reflectivity profiles combined with the PIA_{hydro} parameter. It is of particular interest to asses (1) the validity of SS, (2) the validity of SOSA, and (3) the applicability of the SRT for the estimation of the PIA. The methodology exploits numerical simulations for identifying the PIA_{hydro} ranges where the aforementioned conditions apply. The Monte Carlo model described by Battaglia and Simmer [2008] is particularly suited for such a goal since it can simulate

linearly polarized Gaussian antenna pulsed radar system while accounting for arbitrary scattering order contributions and Kirchoff-type surface returns. Two comments relative to the underlying methodology of the code are as follows.

[8] 1. The adopted approach is phenomenological; that is, we postulate the standard radiative transfer approach (and in particular that the ergodicity and spatial uniformity assumption [see Mishchenko et al., 2006, chapter 8] are fulfilled), so that we can use the quantities such as optical cross sections and scattering/phase matrices. It is still not clear whether or not this is applicable to the case of short-pulse radar illumination.

[9] 2. Backscattering enhancement is accounted for in a naive way by allowing a doubling of the copolar terms for scattering orders higher than 1 [Mishchenko et al., 2006, chapter 8]. This is a conservative estimate: in fact the fast movement of the satellite displaces the return radiation from the exact backscattering direction. A critical discussion about backscattering enhancement in space-borne configuration is provided in section 2.c of Battaglia et al. [2008].

2.1. Sensitivity Study of MS Effects in a Simple Flux-Preserving Model

[10] The Monte Carlo radar simulator has been applied in the CloudSat configuration to simple flux-preserving profiles (see details in section 3 in work by Battaglia and Simmer [2008]). In this work the size distribution of the raindrops is prescribed and the corresponding ice size distribution is derived through the mass-flux preserving assumption with a one-to-one correspondence between ice particles and raindrops. Different exponential drop size distributions (DSD) are considered with $N_0 = 4, 8, 16 \times 10^3 \text{ m}^{-3} \text{ mm}^{-1}$. The microphysics of profiles has been selected as follows: (1) “cold profiles” with different ice microphysics (ice density equal 0.1 and 0.18 g/cm^3); (2) “warm profiles” with no ice at all; and (3) “warm profiles” with “extreme” coexisting liquid water content. The cloud liquid water content is distributed uniformly in a layer located between $0.5 \times H_{FL}$ and $1.5 \times H_{FL}$, H_{FL} being the freezing level altitude; the total liquid water path is related to the rain rate at the ground by the relationship:

$$\min\left(2.0, 0.18 \times \left(1.0 + \sqrt{z_{FL}[\text{km}] \times RR_{ground} [\text{mm/h}]}\right)\right) \text{ [kg/m}^2\text{]}.$$

[11] Figure 2 depicts the departure of the total MS return from the SS/SOS approximation defined as

$$\Delta Z_{SS/SOS}[\text{dB}] \equiv Z_{MS}[\text{dBZ}] - Z_{SS/SOS}[\text{dBZ}] \quad (1)$$

for pixels close to the surface. Precipitating systems with H_{FL} at 2 and 4 km are considered in Figure 2 (top) and Figure 2 (bottom), respectively. Thresholds at 2 dB (equal to the retrieval error expected for PIA_{hydro}) are hereafter assumed to assess the range of validity of the SS/SOS approximations. As expected these approximations become invalid when increasing the one-way PIA_{hydro} . At small PIA_{hydro} (as considered in these plots) the ice microphysics is not important at all; on the other hand the presence of cloud liquid water and/or of small rain droplets strongly

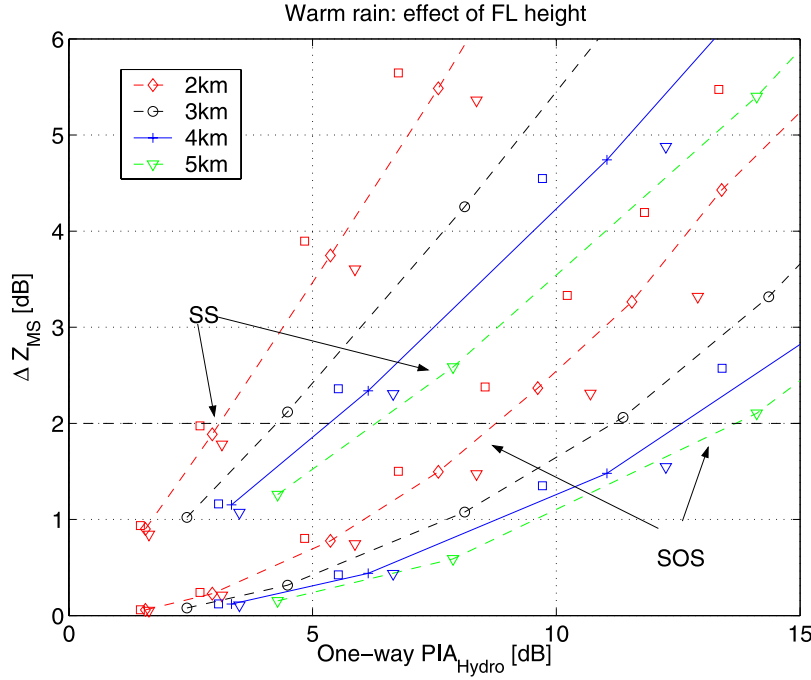


Figure 3. MS enhancement for warm rain with different freezing levels with $N_0 = 8 \times 10^3 \text{ m}^{-3} \text{ mm}^{-1}$ as indicated in the legend. Two groups of curves are plotted: on the left/right side those relative to the SSA/SOSA error. In proximity of the curves corresponding to $H_{FL} = 2$ and 4 km the additional squares and triangles with the same grey scale represent cases with $N_0 = 4, 16 \times 10^3 \text{ m}^{-3} \text{ mm}^{-1}$, respectively.

diminishes MS effects. For instance for systems with a FL at 2 km the SS 2 dB threshold changes from 3 to 5 dB one-way $\text{PIA}_{\text{hydro}}$ when passing from a warm profile to a warm profile with extreme cloud liquid content. This is expected since cloud droplets and/or small raindrops tend to absorb radiation while reducing the SS albedo of the medium.

[12] Note also the substantial gain when looking at the 2 dB threshold of the SOS compared to the SS approximation. For a system with $H_{FL} = 4 \text{ km}$ the 2-dB level is reached at around one-way $\text{PIA}_{\text{hydro}}$ of 5–8 dB while the SOS approximation produces reflectivities within 2 dB for $\text{PIA}_{\text{hydro}}$ between 12 and 17 dB. Finally the consideration of lower freezing levels with the same PIA require in general higher order of scattering (compare Figure 2 top and bottom). This is confirmed in Figure 3 where results are categorized according to the freezing level altitude. In fact, in order to obtain the same $\text{PIA}_{\text{hydro}}$ in a shorter path, higher extinction coefficients are needed, thus lower ratios between the mean free radiation paths and the CloudSat antenna footprint are achieved.

2.2. Assessment of Importance of MS Effects Based on Cloud-Resolving Model Profiles

[13] The simple model used in section 2.1 is useful to identify the main causes of MS enhancements but cannot account for the natural range of variability. Predefined cloud structures may be utilized to overcome this problem. The Goddard Cumulus Ensemble model (GCE), a cloud microphysical model developed mainly by *Tao and Simpson* [1993], is used to supply the required cloud structures.

[14] Reflectivities for CloudSat configuration have been simulated for more than 7000 profiles in fronts, squall lines, hurricanes and extratropical storms with optical thicknesses

between 0 and 20 (i.e., one-way PIA below 86 dB). Figure 4 presents the error produced by the SSA (Figure 4, left) and by the SOSA (Figure 4, right) for the pixels close to the surface for this database (i.e., ranges corresponding to altitudes between 0 and 500 m). Figure 4, top, middle and bottom, refer to profiles with $\text{FL} < 3 \text{ km}$, $3 \text{ km} < \text{FL} < 5 \text{ km}$ and $\text{FL} > 5 \text{ km}$, respectively. As a reference, the color table in Figure 4 (right) indicates the rain rate at the ground. Trends similar to that of Figure 2 are evident: a shifting toward higher FL produces lower SSA and SOSA errors for the same $\text{PIA}_{\text{hydro}}$. When considering a fixed value of the $\text{PIA}_{\text{hydro}}$, the large variability in ΔZ_{SS} and in ΔZ_{SOS} is caused by the differences in the cloud morphologies and in the vertical distribution of the hydrometeors. For instance, when comparing tall systems (represented in our CRM database by hurricanes and squall lines; see Figure 4, bottom), squall lines generally produce more MS owing to a microphysics which favors larger snow and rain particles. In fact large particles tend to have higher SS albedos and more forward-peaked phase functions, thus increasing the radiation path length through the medium and keeping the radiation within the footprint of the instrument. Both these effects are known to enhance MS effects. This microphysical variability leads to the scatter of Figure 4 and will introduce an uncertainty in the flagging thresholds.

[15] Another source of error in the classification may come from outliers characterized by low $\text{PIA}_{\text{hydro}}$ that also necessitate higher orders of scattering for a correct interpretation of the profile. Generally these profiles correspond to drizzle or no rain at the ground but with a considerable amount of ice in the upper layers. As such, they all present a strong peak of reflectivity in some layer and then a steep

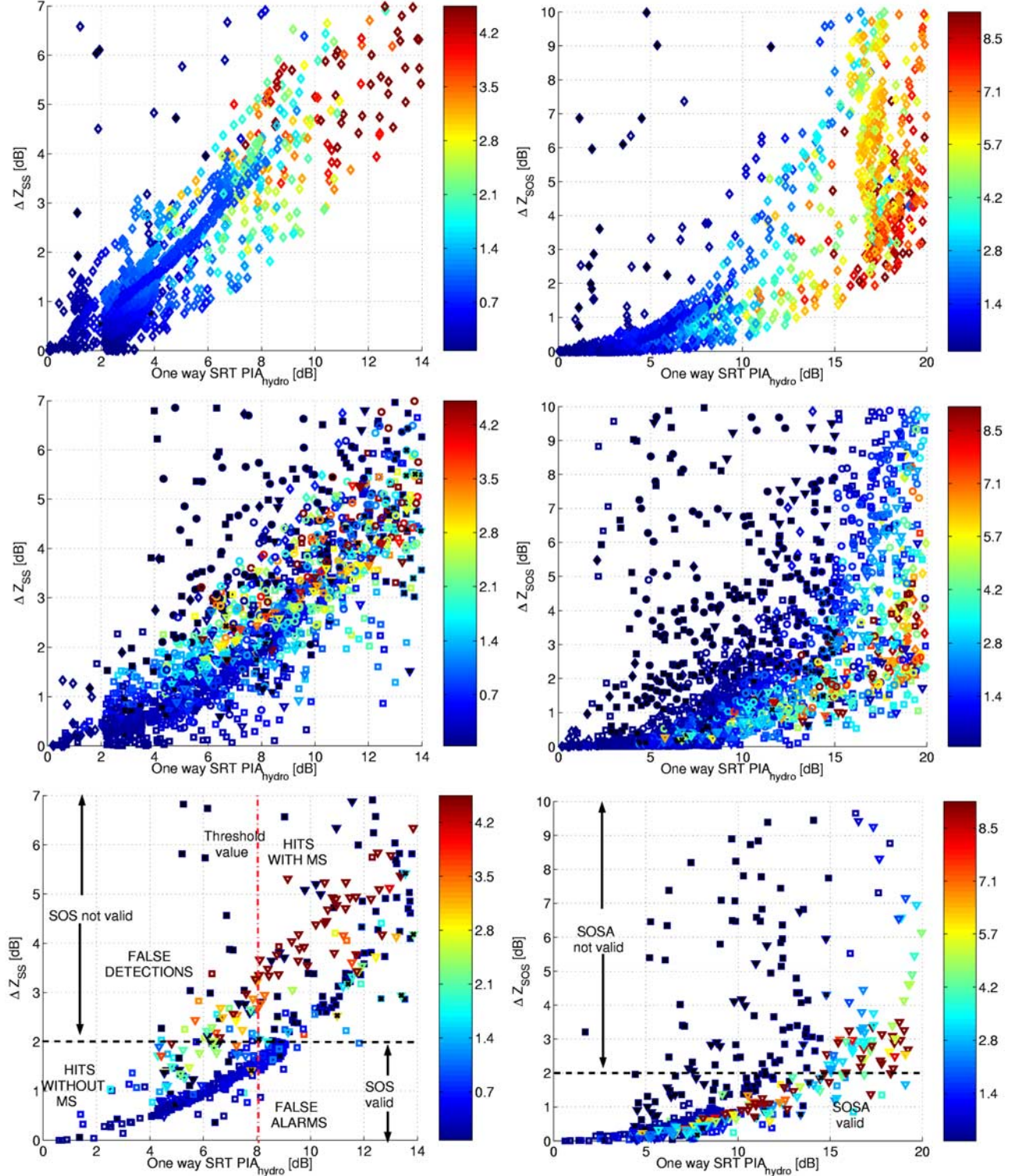


Figure 4. Enhancement of *MS* compared to (left) SSA and (right) SOSA as a function of the one-way hydrometeor PIA (estimated from SRT). The colorbar indicates the rain rate at the ground in mm/h. Diamonds, squares, circles, and triangles correspond to fronts, squall lines, extratropical storms, and hurricanes, respectively. Profiles have (top) $FL < 3$ km, (middle) $3 \text{ km} < FL < 5$ km, and (bottom) $FL > 5$ km. Solid symbols correspond to profiles identified as “outliers” according to the criteria of equations (2)–(3). Profiles with $\Delta Z_{SS} < 2$ dB ($\Delta Z_{SOS} < 2$ dB) may be treated with the SS (SOS) approximation.

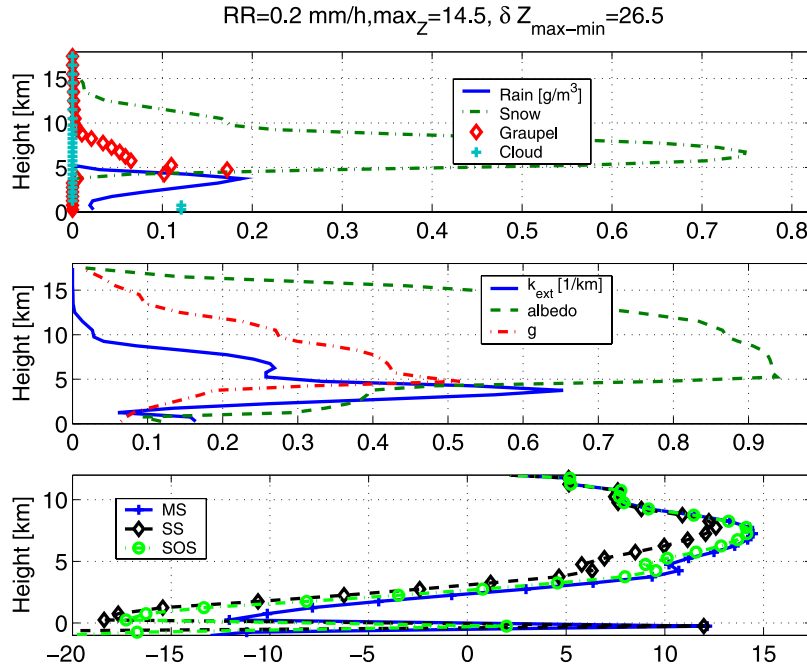


Figure 5. Example of an outlier extracted from Hurricane BOB CRM simulation.

decreasing slope toward the surface. The strong MS component is the result of pulse stretching (see discussion by *Hogan and Battaglia* [2008] and Figure 2 of *Battaglia and Simmer* [2008]). An example of such a profile is provided in Figure 5. In order to identify these outliers thresholds on two parameters have been considered: the maximum value of the reflectivity (\max_Z , which roughly accounts for the presence of ice) and the difference ($\delta Z_{\max-\min}$) between such a maximum and the minimum of the reflectivity values in the vertical profile below the level of the maximum. Many different criteria have been tested on our synthetic database and for each of them the contingency tables with the number of hits of profiles which are (are not) outliers N_A (N_D), the number of false alarms N_B , the number of misses N_C , have been computed. From these parameters, knowing the expected number of correct forecasts due to chance $N_E = (N_A + N_C) \times (N_A + N_B)/N_T$ (where N_T is the total number of profiles), the equitable threat score $ETS \equiv \frac{N_A - N_E}{N_A + N_B + N_C - N_E}$ is computed. The model gets penalized for forecasting outliers in the wrong place as well as not forecasting them in the right place. Thus, the criteria with the highest ETS are generally those with the best forecast skill. The following conditions have been found to fulfill this condition and hence to better identify outliers:

$$\delta Z_{\max-\min} > 21.5 \text{ dB} \text{ when } \max_Z > 10 \text{ dBZ} \& PIA_{hydro} \leq 7 \text{ dB} \quad (2)$$

$$\delta Z_{\max-\min} > 22 \text{ dB} \text{ when } \max_Z > 12 \text{ dBZ} \& 7 < PIA_{hydro} \leq 15 \text{ dB.} \quad (3)$$

2.3. Assessment of Validity of the SRT-PIA Estimates

[16] The evaluation of PIA_{hydro} based on the SRT is correct provided the surface return itself is not totally

obscured owing to MS contamination. As noted by *Battaglia and Simmer* [2008] this condition can be violated in CloudSat observations. Figure 6 shows the simulated PIA_{hydro} based on the SRT versus the PIA_{hydro} directly computed from each profile scattering properties. Results are presented for all CRM profiles discussed in section 2.2. For one-way PIA_{hydro} below 15 dB all scatterpoints are located close to the bisectrix; that is, there is no notable MS obscuration of the surface pixel. On the other hand, for PIA_{hydro} higher than 18–20 dB the one-way SRT based PIA_{hydro} underestimates the real PIA_{hydro} . In addition to the effect of the FL height, the presence of a thick ice layer is a key factor. This was already demonstrated by *Battaglia and Simmer* [2008, Figure 8] where the minimum detection height is strongly lowered moving from a warm rain situation to frontal and substantially more to convective systems with high-density ice particles. Only for this kind of hydrometeors the signal at ranges crossing the surface range becomes decoupled from the surface properties themselves, a clear signal that the radiation backscattered from ranges apparently at the surface distance is not actually sensing the surface itself. A good index for such a situation is given by the “10-dBZ level,” defined as the altitude at which the reflectivity profile reaches a value of 10 dBZ when starting from the FL altitude and moving upward. If such a level is not reached at altitudes above the FL it is then searched for in the lower levels. The color table of Figure 6 indicates the 10-dBZ-level parameter. When profiles with very low 10-dBZ level are considered (small amounts of ice aloft) the applicability of the SRT can be extended to higher values of PIA_{hydro} .

2.4. Threshold Identification

[17] Four distinct scattering regimes can be clearly identified: (1) SS is applicable; (2) SS is unreliable, but SOS is valid; (3) SOS is not valid owing to higher orders of MS

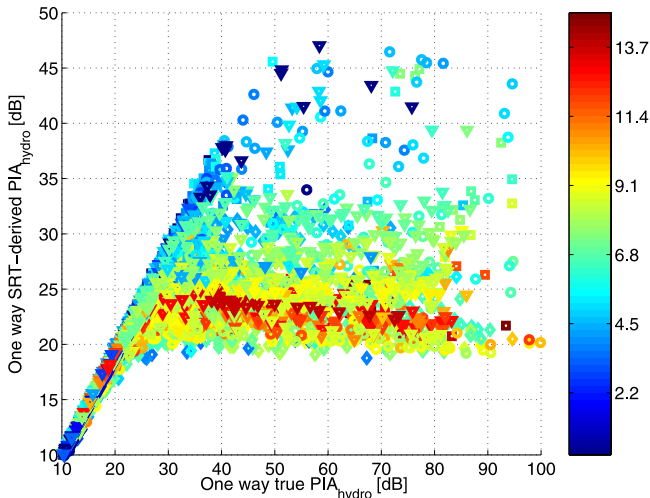


Figure 6. True one-way $\text{PIA}_{\text{hydro}}$ versus one-way SRT-derived $\text{PIA}_{\text{hydro}}$. Diamonds, squares, circles, and triangles correspond to fronts, squall lines, extratropical storms, and hurricanes, respectively. The colorbar indicates the “10-dBZ height above the freezing level” in kilometers (see text for details).

affecting the vertical profile but not affecting SRT-PIA estimates; and (4) MS is affecting also the surface return making the SRT-PIA estimate invalid. These regimes can be separated by three break-point values (see Table 1). The methodology to estimate such threshold values is illustrated in Figure 4 (bottom left): if we adopt the running threshold as an identification criterion of the validity of the SS assumptions, the 2 dB horizontal line and the moving threshold vertical line separate the different simulated profiles in four quadrants: profiles with false detections (left upper quadrant), with false alarms (right lower quadrant) and where the SS and MS are correctly identified (bottom left and top right panels). The threshold value can be selected either by searching for the 99% of probability of detection (POD) or by maximizing the ETS in the available data set of simulations. In each box of Table 1 the two reported values correspond to these two criteria, respectively. The values of the false alarm rate (FAR), POD and ETS based on the contingency table for the detection of CRM profiles where the SS/SOS/SRT approximations are valid/not valid are reported in Table 2 for the whole data set. When the 99% POD level (best ETS) criterion is used high FAR are produced (FAR is still below 17% (10%) when SS and SOSA are considered) but the detection of SRT validity is more problematic with FAR around 40%.

[18] The probability distribution functions of estimated $\text{PIA}_{\text{hydro}}$ for the CloudSat sea-surface pixels affected by rain are shown in Figure 7 (classified according to the freezing level altitudes). The analysis is performed for the period from 15 June 2006 to 18 January 2007. The three arrows indicate the break-point values identified to separate the four scattering regimes. The fractions of CloudSat rainy profiles fulfilling the different conditions on the $\text{PIA}_{\text{hydro}}$ are reported in Table 1 within parentheses. By accounting for the relative frequency of observations of systems with different freezing level altitude, a global statistics for the

CloudSat database can be computed. Approximately 80–85% of the rainy CloudSat profiles can be treated with the SS approximation. An additional 10% can be correctly interpreted, if SOSA is used. Finally, for almost 3.5% of the cases the use of the SRT is questionable.

[19] In Figure 7 note also the presence of a plateau and/or a relative maximum at $\text{PIA}_{\text{hydro}} = 20\text{--}25$ dB which reflects the saturation of the signal of the surface return due to MS effects (in agreement with the behavior in Figure 6 and with the findings of Battaglia and Simmer [2008]). Thus the $\text{PIA}_{\text{hydro}}$ distribution (as derived from SRT) exhibits a bimodal structure especially for taller systems but because of MS effects, it is therefore not possible to conclude that the frequency distribution of surface precipitation is bimodal as well (as previously noted by Haynes and Stephens [2007]). This would have been the case in case of coincidence between true and SRT-derived $\text{PIA}_{\text{hydro}}$.

3. Case Study and Global Statistics

[20] The MS thresholds (Table 1) have been applied to the CloudSat CPR data set. As an illustrative case, the observation of 8 August 2006 (granule 1483) of the Tropical Storm Botha, which occurred close to Taiwan, is examined. The reflectivity panel is shown in Figure 8 (top). The large storm developed up to 16 km in altitude and for almost 800 km across the Pacific Ocean. A strong precipitation core is evident at longitudes between 122.8° and 123.1° (i.e., extending for almost 100 km); in some part of this region the signal falls below the minimum detection threshold. In Figure 8 (bottom) the rain product as derived from AMSR-E (Level 2 product [see Wilheit et al., 2003]) and from the SS-CloudSat algorithm are shown. The SRT-based PIA is plotted as well (with scale reference values in the right axis). The SS-based CloudSat rainfall product clearly shows problems where the rain echo signal disappear, as predicted by L'Ecuyer and Stephens [2002]. In the rain core the algorithm typically underestimates the AMSR-E rainfall product. According to our criteria, the SS-CloudSat estimate is burdened by MS effects; this is highlighted by indicating the two thresholds (see the horizontal dashed lines in Figure 8) for SS and SOS validity proper to the system under consideration (i.e., with a freezing level around 5.5 km) in Figure 8 (bottom). Note also that for all SRT-based PIA exceeding 21 dB the profiles are believed to be MS contaminated (and thus rain generally underestimated). We therefore attribute the above-mentioned SS CloudSat underestimation to MS effects. On the other hand in the first precipitating system (ranging between 122.1° and 122.35°) SS approximation is almost always applicable and retrieved rainfall rates seems to better agree with those from AMSR-E.

Table 2. FAR, POD, and ETS for the CRM Database

Case	POD	ETS	FAR
SSA (99% POD threshold)	0.99	0.53	0.13
SSA (best-ETS threshold)	0.96	0.71	0.06
SOSA (99% POD threshold)	0.99	0.61	0.17
SOSA (best-ETS threshold)	0.97	0.73	0.10
SRT (99% POD threshold)	0.99	0.41	0.42
SRT (best-ETS threshold)	0.97	0.46	0.38

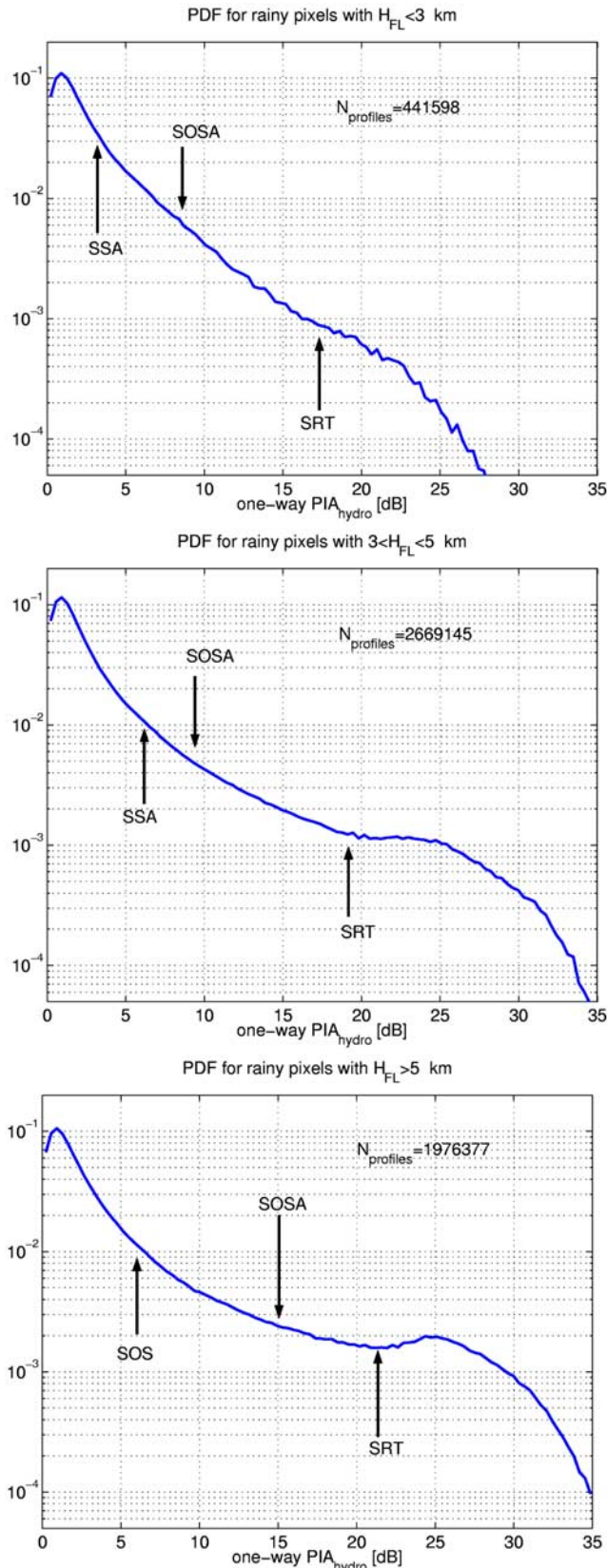


Figure 7. Probability distribution function of $\text{PIA}_{\text{hydro}}$ estimated by the SRT for rainy sea-surfaces pixels in the CloudSat database. The arrows indicate the 99% POD thresholds given in Table 1. The analysis covers the period from 15 June 2006 to 18 January 2007.

[21] The results reported in Figure 7 represent global statistics for all raining system with different freezing level altitudes observed by the CloudSat CPR. However, owing to the different precipitation systems, results are strongly regionally and seasonally dependent. The three panels of Figure 9 present global maps of the fraction of raining scenes during the period from December 2006 to February 2007 in which the SS approximation is valid, the SOSA is required and sufficient and in which higher orders of scattering are required. The three panels sum up to unity. In Figure 9 (bottom) the highest values are found along the storm tracks and especially in the Inter Tropical Convergence Zone. In some of these regions, higher than second orders of scattering must be applied to 15–25% of the cases. Similarly Figure 10 depicts global maps of the fraction of raining scenes in which the PIA has been correctly estimated by the SRT. Again, as expected, the lowest values are found along the storm tracks of the midlatitudes and in the Inter Tropical Convergence Zone. The SRT is almost always true in the East Pacific while it can be invalid for more than 15–20% of the rainy cases in some regions of the West Pacific. This reflects the different types of systems that give rise to rainfall in these two areas [Masunaga et al., 2005]. By comparing Figure 10 (top) (DJF) and (bottom) (JJA), the seasonal variation of such systems can be observed as well; note the strong signature in the SW Pacific, in the SW Atlantic and in the SW Indian Ocean during DJF and in the NW Pacific and in the NW Atlantic during JJA. Zonal means are presented in Figure 11: in the equatorial zone the SS approximation can be used in rainy condition for 70–75% of the time; the remaining cases must be treated with SOSA (15–20%) or even higher order of scattering theories (10%). Moving away from the equator, the validity of the SS generally widens, except for the presence of extratropical cyclones (see the bumps at $+30^{\circ}$ latitude during DJF and at around -35° latitude during JJA). In the Northern Hemisphere at 60°N SS is enough to represent CloudSat profiles for 90% (95%) of the times during summertime (wintertime) and only a few percentage of the profiles needs higher order of scattering.

[22] Obviously higher rain rates are associated with precipitation features that explain much of the total rainfall (in particular in the tropics). A companion paper by Haynes et al. (submitted manuscript, 2008) takes a first look at quantifying this problem and demonstrates the CPR does, in fact, underestimate tropical rainfall.

4. Conclusions

[23] The probability of MS effects in CloudSat Profiling Radar reflectivity measurements when overpassing precipitation systems necessitates criteria to identify affected profiles prior to any rain retrieval algorithm. We propose a flagging criterion which relies on the PIA estimated via the SRT, a product available in the 2B-GEOPROF. On the basis of numerical simulation of a large variety of Cloud Resolving Model-generated microphysical profiles, depending on the freezing level altitude, three different PIA breakpoint values delineate different four scattering regimes as summarized in Table 1. Outliers can also be identified by using simple conditions derivable from the reflectivity

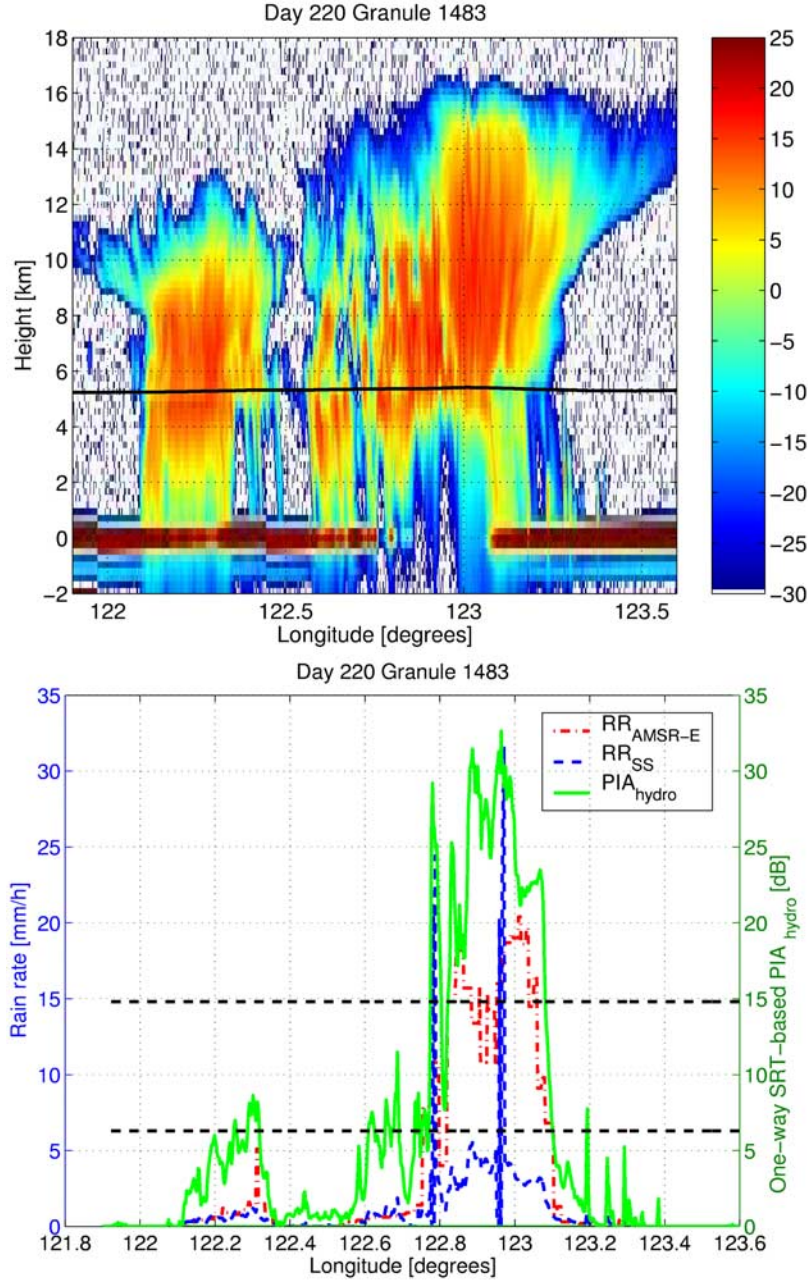


Figure 8. Case study for Tropical storm Bopha. (top) CPR reflectivities in dBZ; (bottom) estimated rain rates near surface from the SS-based CloudSat algorithm and from the collocated AMSR-E product and SRT-based estimated PIA.

profiles (see equations (2) and (3)). With our criteria it is straightforward to detect whether the profiles can be treated with the SS or need the application of SOSA. Note that the results of Table 1 are somehow based on arbitrary freezing level classes. However, without sticking to ad hoc thresholds, by adopting a conservative approach in relation to the results of Figure 4 we can conclude that the SS approximation is valid for $\text{PIA}_{\text{hydro}}$ lower than 3 (low) to 5.5 dB (tall systems) while the SOS approximation is applicable to profiles with $\text{PIA}_{\text{hydro}}$ lower than 8 (low) to 9 dB (tall).

[24] Thresholds for the validity of the SRT-based PIA estimate are defined as well. For one-way $\text{PIA}_{\text{hydro}}$ above 19–21 dB especially in presence of tall systems with high

reflectivities aloft (see Figure 6) the real $\text{PIA}_{\text{hydro}}$ can be easily underestimated by many tens of dB. These thresholds should always be applied to CloudSat data whenever the interpretation of radar returns in precipitating regions is required. In addition to rainfall retrievals, applications involving the comparison of CloudSat reflectivity observations with CRM-based simulations or ground-based radars that operate at different frequency or even the comparison of CloudSat reflectivity histograms in different regions or climate regimes may be adversely affected if the presence of multiple scattering is not accounted for.

[25] Global statistics of the occurrence of multiple scattering is presented: for ocean pixels, roughly speaking

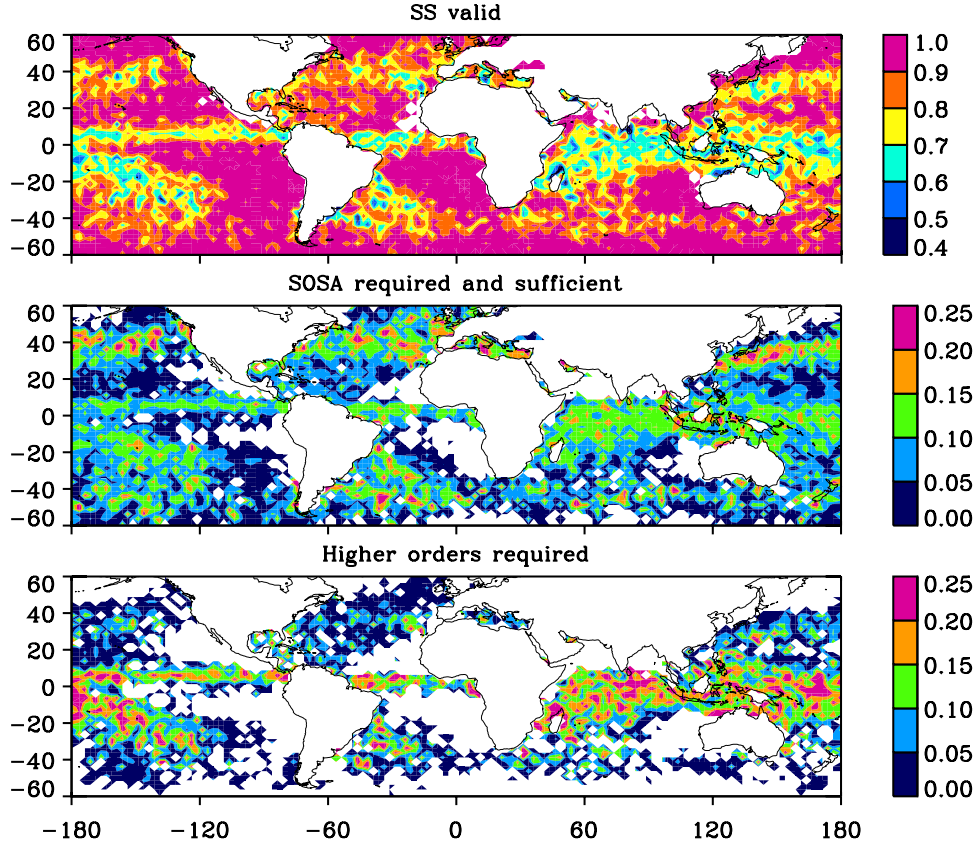


Figure 9. Global maps of the fraction of raining scenes during the period from December 2006 to February 2007 in which (top) the SS approximation is valid, (middle) the SOSA is required and sufficient, and (bottom) higher orders of scattering are required.

(detailed results are reported in Table 1) around 80% (90%) of the profiles identified as rainy can be treated with the SS (SOS) approximation. But for 3.5% of the rainy pixels even the PIA estimate is unreliable. Owing to the different precipitation regimes, the frequency with which MS effects

are encountered is strongly regionally and seasonally dependent. CloudSat CPR reflectivity profiles have to be more frequently treated with higher order of scattering theories in presence of the highly developed and optically thick systems, frequently found in the InterTropical

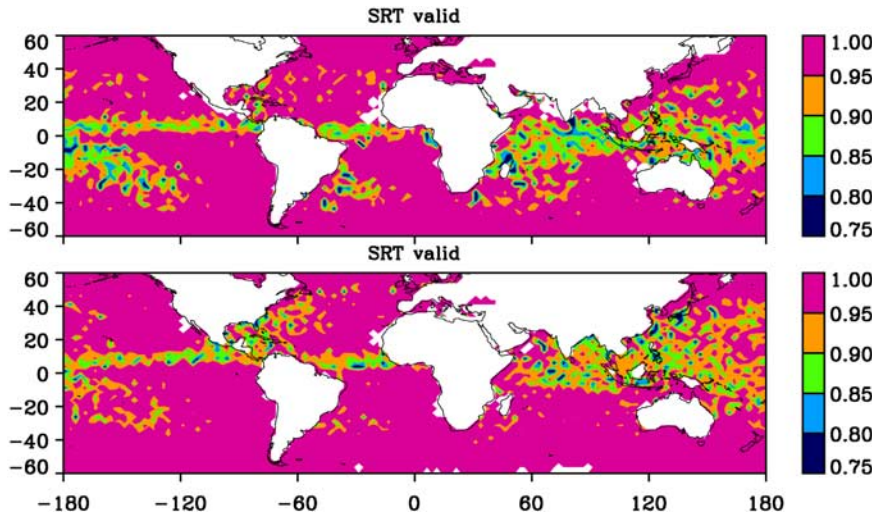


Figure 10. Global maps of the fraction of raining scenes during the period (top) from December 2006 to February 2007 and (bottom) from June 2006 to August 2006 in which the PIA can be correctly estimated by the SRT.

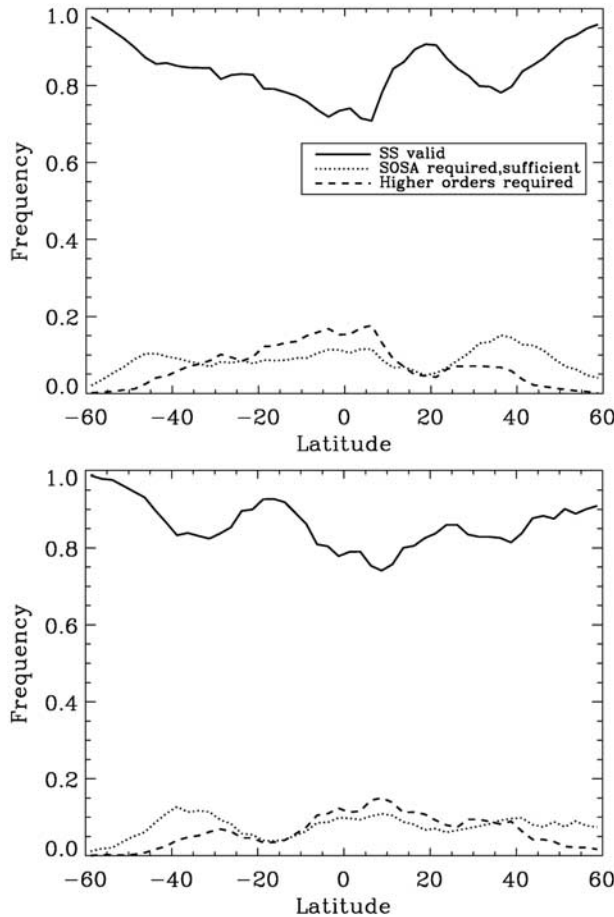


Figure 11. (top) Zonal mean of the data presented in Figure 9. (bottom) Same for the JJA period.

Convergence Zone and in the tracks of extratropical cyclones. In the equatorial zone the SS approximation can be used in rainy condition only in 75–80% of the time; the remaining cases must be treated with SOSA (10–15%) or even with higher order of scattering theories (~10%). Away from the equator the validity of the SS generally widens: in the Northern Hemisphere at 60°N the SSA is sufficient to interpret rainy CloudSat profiles for 90% (95%) of the times during summertime (wintertime) and only less than 4% of the profiles need higher order of scattering.

[26] **Acknowledgments.** The development of the CloudSat precipitation data set from which PIA was extracted is funded under NASA Grant NNX07AR97G. The work performed by A. Battaglia has been partially funded by the German Science Foundation under the TOSCA project. The authors would like to thank Simone Tanelli (JPL) for his help and productive discussions during the course of the research.

References

- Battaglia, A., and C. Simmer (2008), How does multiple scattering affect the spaceborne W-band radar measurements at ranges close to and crossing the sea-surface range?, *IEEE Trans. Geosci. Remote Sens.*, **46**(6), 1644–1651.
- Battaglia, A., M. O. Ajewole, and C. Simmer (2005), Multiple scattering effects due to hydrometeors on precipitation radar systems, *Geophys. Res. Lett.*, **32**, L19801, doi:10.1029/2005GL023810.
- Battaglia, A., M. O. Ajewole, and C. Simmer (2006a), Evaluation of radar multiple scattering effects from a GPM perspective. Part I: Model description and validation, *J. Appl. Meteorol.*, **45**(12), 1634–1647.
- Battaglia, A., M. O. Ajewole, and C. Simmer (2006b), Evaluation of radar multiple scattering effects from a GPM perspective. Part II: Model results, *J. Appl. Meteorol.*, **45**(12), 1648–1664.
- Battaglia, A., M. O. Ajewole, and C. Simmer (2007), Evaluation of radar multiple scattering effects in CloudSat configuration, *Atmos. Chem. Phys.*, **7**, 1719–1730.
- Battaglia, A., S. Kobayashi, S. Tanelli, E. Im, and C. Simmer (2008), Multiple scattering effects in pulsed radar systems: An intercomparison study, *J. Atmos. Oceanic Technol.*, **25**, 1556–1567.
- Haynes, J. M., and G. L. Stephens (2007), Tropical ocean cloudiness and the incidence of precipitation: Early results from CloudSat, *Geophys. Res. Lett.*, **34**, L09811, doi:10.1029/2007GL029335.
- Hogan, R. J., and A. Battaglia (2008), Fast lidar and radar multiple-scattering models: Part 2: Wide-angle scattering using the time-dependent two-stream approximation, *J. Atmos. Sci.*, doi:10.1175/2008JAS2643.1, in press. (Available at <http://ams.allenpress.com/perlerv/?request=get-abstract&doi=10.1175/2008JAS2643.1>)
- Iguchi, T., T. Kozu, R. Meneghini, J. Awaka, and K. Okamoto (2000), Rain-profiling algorithm for the TRMM precipitation radar, *J. Appl. Meteorol.*, **39**(12), 2038–2052.
- Iguchi, T., R. Oki, E. A. Smith, and Y. Furuhama (2002), Global precipitation measurement program and the development of dual-frequency precipitation radar, *J. Commun. Res. Lab.*, **49**(2), 37–45.
- Kobayashi, S., S. Tanelli, and E. Im (2005), Second-order multiple-scattering theory associated with backscattering enhancement for a millimeter wavelength weather radar with a finite beam width, *Radio Sci.*, **40**, RS6015, doi:10.1029/2004RS003219.
- Kobayashi, S., S. Ito, S. Tanelli, T. Oguchi, and E. Im (2007), A time-dependent multiple scattering theory for a pulsed radar with a finite beam width, *Radio Sci.*, **42**, RS4001, doi:10.1029/2006RS003555.
- Kummerow, C. D., W. Barnes, T. Kozu, J. Shiue, and J. Simpson (1998), The tropical rainfall measuring mission (TRMM) sensor package, *J. Atmos. Oceanic Technol.*, **15**(3), 809–817.
- L'Ecuyer, T. S., and G. L. Stephens (2002), An estimation-based precipitation retrieval algorithm for attenuating radars, *J. Appl. Meteorol.*, **41**(3), 272–285.
- Lhermitte, R. (1990), Attenuation and scattering of millimeter wavelength radiation by clouds and precipitation, *J. Atmos. Oceanic Technol.*, **7**(3), 464–479.
- Li, L., G. M. Heymsfield, P. E. Racette, L. Tian, and E. Zenke (2004), A 94-GHz cloud radar system on a NASA high-altitude ER-2 aircraft, *J. Atmos. Oceanic Technol.*, **21**(9), 1378–1388.
- Mace, G. G., R. Marchand, Q. Zhang, and G. Stephens (2007), Global hydrometeor occurrence as observed by CloudSat: Initial observations from summer 2006, *Geophys. Res. Lett.*, **34**, L09808, doi:10.1029/2006GL029017.
- Marzano, F. S., L. Roberti, S. Di Michele, A. Mugnai, and A. Tassa (2003), Modeling of apparent radar reflectivity due to convective clouds at attenuating wavelengths, *Radio Sci.*, **38**(1), 1002, doi:10.1029/2002RS002613.
- Masunaga, H., and C. D. Kummerow (2005), Variability in the characteristics of tropical precipitation systems. Part I: Spatial structure, *J. Clim.*, **18**, 823–840.
- Matrosov, S. Y. (2007), Potential for attenuation-based estimation of rainfall rate from CloudSat, *Geophys. Res. Lett.*, **34**, L05817, doi:10.1029/2006GL029161.
- Matrosov, S. Y., A. Battaglia, and P. Rodriguez (2008), Effects of multiple scattering on attenuation-based retrievals of stratiform rainfall from CloudSat, *J. Atmos. Oceanic Technol.*, doi:10.1175/2008JTECHA1095, in press. (Available at <http://ams.allenpress.com/perlerv/?request=get-abstract&doi=10.1175/2008JTECHA1095.1>)
- Meneghini, R., T. Iguchi, T. Kozu, L. Liao, K. Okamoto, J. A. Jones, and J. Kwiatkowski (2000), Use of the surface reference technique for path attenuation estimates from the TRMM precipitation radar, *J. Appl. Meteorol.*, **39**(12), 2053–2070.
- Meneghini, R., J. A. Jones, T. Iguchi, K. Okamoto, and J. Kwiatkowski (2004), A hybrid surface reference technique and its application to the TRMM precipitation radar, *J. Atmos. Oceanic Technol.*, **21**(11), 1645–1658.
- Mishchenko, M. I., L. D. Travis, and A. A. Lacis (2006), *Multiple Scattering of Light by Particles: Radiative Transfer and Coherent Backscattering*, 494 pp., Cambridge Univ. Press, Cambridge, U.K.
- Mitrescu, C., J. Haynes, T. L'Ecuyer, S. Miller, and J. Turk (2007), Light rain retrievals using CloudSat 94-GHz radar data—Preliminary results, paper presented at 87th Annual Meeting, Am. Meteorol. Soc., San Antonio, Tex.
- Mitrescu, C., S. Miller, J. Hawkins, T. L'Ecuyer, J. Turk, P. Partain, and G. L. Stephens (2008), Near-real-time applications of CloudSat data, *J. Appl. Meteorol.*, **47**(7), 1982–1994.
- Pujol, O., J.-F.-A. Georgis, L. Feral, and H. Sauvageot (2007), Degradation of radar reflectivity by cloud attenuation at microwave frequency, *J. Atmos. Oceanic Technol.*, **24**(4), 640–657, doi:10.1175/JTECH1992.1.

- Stephens, G. L., et al. (2002), The CloudSat mission and the A-train, *Bull. Am. Meteorol. Soc.*, 83(12), 1771–1790.
- Tanelli, S., S. Durden, E. Im, K. Pak, D. Reinke, P. Partain, J. Haynes, and R. Marchand (2008), CloudSat's cloud profiling radar after 1 year in orbit: Performance, calibration, and processing, *IEEE Trans. Geosci. Remote Sens.*, in press.
- Tao, W. K., and J. Simpson (1993), Goddard Cumulus Ensemble Model, Part I: Model description, *Terr. Atmos. Oceanic Sci.*, 4, 35–72.
- Wilheit, T., C. Kummerow, and R. Ferraro (2003), Rainfall algorithms for AMSR-E, *IEEE Trans. Geosci. Remote Sens.*, 41(2), 204–214.

A. Battaglia and C. Simmer, Department of Meteorology, University of Bonn, Auf dem Hugel, 20, D-53121 Bonn, Germany. (batta@uni-bonn.de)
J. M. Haynes and T. L'Ecuyer, Department of Atmospheric Sciences, Colorado State University, Fort Collins, CO 80523-1371, USA.